5. Resistivity frequency dispersion effects

Most of the MT soundings showed some discrepancies with the synthetic MT diagrams derived from the DES data, suggesting the possible influence of induced polarisation phenomena. A Cole-Cole dispersion model (Pelton *et al.*, 1978) was used to fit the data, and the obtained sets of dispersion parameters, namely chargeability m, time constant τ and frequency factor c, are reported in table I.

Following the interpretation approach described in a recent paper (Mauriello *et al.*, 1996), the chargeability and time constant parameters seem to play the most important role for the evaluation of the dispersion effects in volcanic areas. In particular, the chargeability may be related to the degree of alteration and mineral particle deposition due to volcanic rock-fluid interaction, while the time constant may be mostly regulated by the local existing temperature. Therefore, the high chargeability values reported in table I (greater than 0.9) would indicate that abundant alteration by-products were formed in both the northern and southern sectors of the investigated area. Time constants exceptionally of a few hundreds of seconds in the northern part (MT15 and MT16), but normally not greater than a few tens of seconds, would instead be indicative of low temperatures in the first 500 m of depth. We may thus conclude that the two sectors, more than other places in the Etnean area, would likely have been involved in magma uprising, but no long-standing active thermal source would be present in the shallow crust, and hence no thermal effect in the form of long relaxation times would be set up. This conclusion can also be drawn from the diagram of fig. 12, where an empirical time constant-temperature correlation is reported, which was derived from the analysis of other case-histories, under partially or totally controlled volcano-geothermal conditions (Coppola *et al.*, 1993; Giammetti *et al.*, 1996). Indeed, as reported in fig. 12, for the Mt. Etna case temperatures not higher than 100 °C, but most probably below 50 °C, would correspond to the polarisable layers.

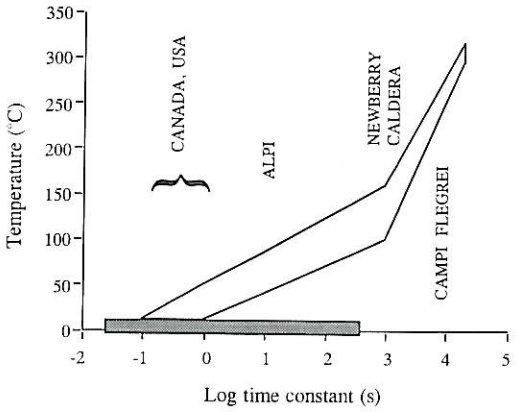

Fig. 12. Temperature *versus* Cole-Cole time constant empirical diagram. The shaded strip is the interval where the time constants estimated at Mt. Etna are included.

6. Conclusions

We have shown the results of a magnetotelluric (MT) study performed in the volcanic area of Mt. Etna (Sicily, Italy) and given an approach to the structural interpretation by comparing the new MT data with previous deep dipole geoelectrical soundings (DES) and passive seismic tomographies.

In particular, the MT-DES integration fully conforms to a previous DES model elaborated down to 3-5 km depth and strengthen the hypothesis that no permanent magma chamber should exist in the shallow crust (Loddo *et al.*, 1989). This conclusion is in fact supported by a study of the resistivity frequency dispersion effects. Temperatures not higher than 100 °C, most probably below 50 °C, would correspond to the dispersive layers, whose short relaxation times would be indicative of the absence of a long-standing shallow thermal source.

The comparison with the shallow seismic tomographies in the central area of the volcanic complex in the depth range from sea level down to about 8 km (Hirn *et al.*, 1991) singles out a zone of slowly cooled compact dikes, surrounded by fractured volcanics, with alteration phenomena mainly concentrated in the upper eastern side. A physical support to this last conclu-

sion is again given by the conformal distribution of significant resistivity frequency dispersion effects in the same area.

The comparison with the 3D interpretation of a regional earthquakes and teleseisms data set (Sharp *et al.*, 1980) shows that only a rough low resistivity-low velocity correlation exists in the studied area in the depth range 15-25 km. The MT data highlight the presence of an E-W elongated resistive body, which has no equivalent in the seismic model. This resistive barrier separates two conductive zones, which are associated with two independent volcanic feeding systems. Accounting for the estimated conductivity values, at least the southern conductor can be interpreted as a partially molten zone with an estimated melt fraction of about 12-16%.

Finally, a good correlation appears between the outlined MT model and the volcanic and seismological patterns. Indeed, the localization of the deepest conductors reflects the surface distribution of the eccentric volcanoes, and the hypocentres distribution of the seismic activity before the 1991-1993 eruption clusters inside the high resistivity barrier.

Concluding, we wish to address the point that we are well aware of the rather limited nature of the adopted 1D MT interpretation scheme as far as it relates to the lateral geometrical bounds within the model. In principle, the correct use of a standard 3D modelling algorithm requires the knowledge of the actual regional electric pattern surrounding the study area (Mackie *et al.*, 1993). However, in an insular area like Sicily, where adequate boundary constraints can hardly be achieved also because of a largely dominant complex geology, such a 3D modelling is likely to give ambiguous or even unreliable results.

Acknowledgements

Study performed with the financial support of the Commission of the European Communities, ETNATECH project, contract EV5V-CT92-0191, and from the Italian Group of Volcanology, National Research Council.

REFERENCES

BARBERI, F., P. GASPARINI, F. INNOCENTI and L. VILLARI (1973): Volcanism of the Southern Tyrrhenian Sea and its geodynamic implications, *J. Geophys. Res.*, **78**, 5221-5232.

BONACCORSO, A., F. FERRUCCI, D. PATANÈ and L. VILLARI (1996): Fast deformation processes and eruptive activity at Mount Etna (Italy), *J. Geophys. Res.*, **101**, 17467-17480.

BOSTICK, F.X. JR. (1977): A simple and almost exact method of MT analysis, in *Workshop on Electrical Methods in Geothermal Exploration, Snowbird, Utah, 1976* (abstract).

CASSINIS, R., I. FINETTI, P. GIESE, C. MORELLI, L. STEINMETZ and O. VECCHIA (1969): Deep seismic refraction research on Sicily, *Boll. Geofis. Teor. Appl.*, **11**, 140-160.

COLOMBI, B., I. GUERRA, G. LUONGO and S. SCARASCIA (1979): Profilo sismico a rifrazione Acireale-Termini Imerese, in *Atti Convegno P.F. Geodinamica. Contributi Preliminari alla Sorveglianza e Rischio Vulcanico (Etna-Eolie), Pubblication* No. 235, 155-170.

CONDOMINES, M., J.C. TANGUY, G. KIEFFER and C.J. ALLÈGRE (1982): Magmatic evolution of a volcano studied by ^{230}Th-^{238}U disequilibrium and trace element systematics: the Etna case, *Geochim. Cosmochim. Acta*, **46**, 1397-1416.

COPPOLA, B., R. DI MAIO, I. MARINI, A. MERLA, D. PATELLA, G. PULELLI, F.M. ROSSI and A. SINISCALCHI (1993): Study of the Simplon area geothermal anomaly in the frame of a transalpine deep railway tunnel feasibility project, in *Underground Transportation Infrastructures, Proceedings of an International Conference of the French Association of Underground Works, Toulon, 1993*, edited by J.L. REITH (Balkema Publishers, Rotterdam), 93-102.

COSENTINO, M., G. LOMBARDO, G. PATANÈ, R. SCHICK and A.D.L. SHARP (1982): Seismological researches on Mount Etna: state of art and recent trends, *Mem. Soc. Geol. It.*, **23**, 159-202.

DI MAIO, R., P. MAURIELLO, D. PATELLA, Z. PETRILLO, S. PISCITELLI and A. SINISCALCHI (1998): Electric and electromagnetic outline of the Mount Somma-Vesuvius structural setting, *J. Volcanol. Geotherm. Res.*, **82**, 219-238.

GIAMMETTI, S., D. PATELLA, A. SINISCALCHI and A. TRAMACERE (1996): The Siena Graben: combined interpretation of DES and MT soundings, *Ann. Geofis.*, **39** (1), 189-200.

HIRN, A., A. NERCESSIAN, M. SAPIN, F. FERRUCCI and G. WITTLINGER (1991): Seismic hetereogenity of Mt. Etna: structure and activity, *Geophys. J. Int.*, **105**, 139-153.

HÖRDT, A., H. JÖDICKE, K.-M. STRACK, K. VOZOFF and P.A. WOLFGRAM (1992): Inversion of long-offset TEM soundings near the borehole Münsterland 1, Germany, and comparison with MT measurements, *Geophys. J. Int.*, **108**, 930-940.

INGHAM, M.R. (1988): The use of invariant impedances in magnetotelluric interpretation, *Geophys. J. Int.*, **92**, 165-169.

INGHAM, M.R. (1992): Audiomagnetotelluric soundings on

White Island volcano, *J. Volcanol. Geotherm. Res.*, **50**, 301-306.

KELLETT, R.L., M. MARESCHAL and R.D. KURTZ (1992): A model of lower crustal electrical anisotropy for the Pontiac Subprovince of the Canadian shield, *Geophys. J. Int.*, **111**, 141-150.

LENTINI, F. (1982): The geology of the Mt.Etna basement, *Mem. Soc. Geol. It.*, **23**, 7-25.

LODDO, M., D. PATELLA, R. QUARTO, G. RUINA, A. TRAMACERE and G. ZITO (1989): Application of gravity and deep dipole geoelectrics in the volcanic area of Mt. Etna (Sicily), *J. Volcanol. Geotherm. Res.*, **39**, 17-39.

MACKIE, R.L., T.R. MADDEN and P.E. WANNAMAKER (1993): Three-dimensional magnetotelluric modeling using difference equations – Theory and comparisons to integral equation solutions, *Geophysics*, **58**, 215-226.

MAURIELLO, P., D. PATELLA and A. SINISCALCHI (1996): The magnetotelluric response over 2D media with resistivity frequency dispersion, *Geophys. Prospect.*, **44**, 789-818.

MAURIELLO, P., D. PATELLA, Z. PETRILLO and A. SINISCALCHI (1997): Mount Etna structural exploration by magnetotellurics, *Acta Volcanologica*, **9**, 1-6.

NAGY, Z. (1996): Advances in the combined interpretation of seismics with magnetotellurics, *Geophys. Prospect.*, **44**, 1041-1083.

OLHOEFT, G.R. (1981): Electrical properties of granite with implications for the lower crust, *J. Geophys. Res.*, **86**, 931-936.

PARK, S.K. and D.W. LIVELYBROOKS (1989): Quantitative interpretation of rotationally invariant parameters in magnetotellurics, *Geophysics*, **54**, 1483-1490.

PARKER, R.L. and J.R. BOOKER (1996): Optimal one-dimensional inversion and bounding of magnetotelluric apparent resistivity and phase measurements, *Phys. Earth Planet. Inter.*, **98**, 269-282.

PATANÈ, D., E. PRIVITERA, F. FERRUCCI and S. GRESTA (1994): Seismic activity leading to the 1991-93 eruption of Mt. Etna and its tectonic implications, *Acta Volcanologica*, **4**, 47-56.

PATELLA, D. (1987): Tutorial: interpretation of magnetotelluric measurements over an electrically dispersive one-dimensional earth, *Geophys. Prospect.*, **35**, 1-11.

PATELLA, D. (1993): I principi metodologici della magnetotellurica su mezzi generalmente dispersivi, *Ann. Geofis.*, **36** (suppl. n. 5-6), 147-160.

PATELLA, D., A. TRAMACERE, R. DI MAIO and A. SINISCALCHI (1991): Experimental evidence of resistivity frequency-dispersion in magnetotellurics in Newberry (Oregon), Snake River Plain (Idaho) and Campi Flegrei (Italy) volcano-geothermal areas, *J. Volcanol. Geotherm. Res.*, **48**, 61-75.

PELTON, W.H., S.H. WARD, P.G. HALLOF, W.R. SILL and P.H. NELSON (1978): Mineral discrimination and removal of inductive coupling with multifrequency IP, *Geophysics*, **43**, 588-609.

RANGANAYAKI, R.P. (1984): An interpretative analysis of magnetotelluric data, *Geophysics*, **49**, 1730-1748.

RITTMANN, A. (1973): Structure and evolution of Mount Etna, *Philos. Trans. R. Soc. London*, **274**, 5-16.

SCANDONE, P., G. GIUNTA and V. LIGUORI (1977): The connection between the Apulia and Sahara continental margins in the Southern Apennines and in Sicily, *Mem. Soc. Geol. It.*, **13**, 317-323.

SHANKLAND, T.J. and M.E. ANDER (1983): Electrical conductivity, temperatures and fluids in the lower crust, *J. Geophys. Res.*, **88**, 9475-9484.

SHANKLAND, T.J., R.J. O'CONNELL and H.S. WAFF (1981): Geophysical constraints on partial melt in the upper mantle, *Rev. Geophys.*, **198**, 394-406.

SHARP, A.D.L. (1982): Deep seismic sounding at Mount Etna, *Mem. Soc. Geol. It.*, **23**, 197-205.

SHARP, A.D.L., P.M. DAVIS and F. GRAY (1980): A low velocity zone beneath Mount Etna and magma storage, *Nature*, **287**, 587-591.

SIMS, W.E., F.X. BOSTICK JR. and H.W. SMITH (1971): The estimation of magnetotelluric impedance tensor elements from measured data, *Geophysics*, **36**, 938-942.

SWIFT, C.M. JR. (1967): A magnetotelluric investigation of an electrical conductivity anomaly in the Southwestern United States, *Ph.D. Thesis*, M.I.T., Boston.

TANGUY, J.C., M. CONDOMINES and G. KIEFFER (1997): Evolution of the Mount Etna magma: constraints on the present feeding system and eruptive mechanism, *J. Volcanol. Geotherm. Res.*, **75**, 221-250.

TORRES-VERDÍN, C. and F.X. BOSTICK JR. (1992): Principles of spatial surface electric field filtering in magnetotellurics: electromagnetic array profiling (EMAP), *Geophysics*, **57**, 603-622.

VOZOFF, K. (1972): The magnetotelluric method in the exploration of sedimentary basins, *Geophysics*, **37**, 98-141.

VOZOFF, K. and D.L.B. JUPP (1975): Joint inversion of geophysical data, *Geophys. J. R. Astron. Soc.*, **42**, 977-991.

WAFF, H.S. (1974): Theoretical considerations of electrical conductivity in a partially molten mantle and implications for geothermometry, *J. Geophys. Res.*, **79**, 4003-4010.

WANNAMAKER, P.E., G.W. HOHMANN and S.H. WARD (1984): Magnetotelluric responses of three-dimensional bodies in layered earth, *Geophysics*, **49**, 1517-1533.

WEAVER, J.T. and A.K. AGARWAL (1993): Automatic 1-D inversion of magnetotelluric data by the method of modelling, *Geophys. J. Int.*, **112**, 115-123.

ZHDANOV, M.S. and G.V. KELLER (1994): *The Geoelectrical Methods in Geophysical Exploration* (Elsevier, Amsterdam), pp. 873.

ZHDANOV, M.S., P. TRAYNIN and J.R. BOOKER (1996): Underground imaging by frequency-domain electromagnetic migration, *Geophysics*, **61**, 666-682.

A physical pattern recognition approach for 2D electromagnetic induction studies

Paolo Mauriello ([1]) **and Domenico Patella** ([2])
([1]) *Istituto per le Tecnologie Applicate ai Beni Culturali, CNR, Roma, Italy*
([2]) *Dipartimento di Scienze Fisiche, Università «Federico II», Napoli, Italy*

Abstract
We present a new tomographic procedure for the analysis of natural source electromagnetic (EM) induction field data collected over any complex 2D buried structure beneath a flat air-earth boundary. The tomography is developed in a pure physical context and the primary goal is the depiction of the space distribution of two occurrence probability functions for the induced electrical charge accumulations on resistivity discontinuities and current channelling inside conductive bodies, respectively. The procedure to obtain tomographic images consists of a scanning operation governed analytically by a set of multiple interference cross-correlations between the observed EM components and the corresponding synthetic components of a pair of elementary charge and dipole. To show the potentiality of the proposed physical tomography, we discuss the results from three 2D synthetic examples.

Key words *electromagnetic induction – pattern recognition – 2D structures*

1. Introduction

The interpretation of natural source electromagnetic (EM) induction field data over complex earth's structures is one of the most difficult problems in applied geophysics. Forward and inverse modelling are still common approaches, but tomographic imaging is the method that is increasingly gaining interest in current researches.

EM Tomography (EMT) started following the principles of acoustic imaging that is a high-resolution method requiring a high density of acquisition sites. Acoustic tomography was largely stimulated for its ability to provide a detailed signature of any complex structure. EMT is however still limited to 2D structures. Significant results about EMT can be found in Lee *et al.* (1987, 1989), Eaton (1989), Sasaki (1989), Poulton *et al.* (1992), Zhou *et al.* (1993), Sasaki *et al.* (1994) and Zhdanov *et al.* (1996).

In this paper we propose a new 2D EMT method, which is completely different from previous methods both conceptually and practically. We do not require any *a priori* knowledge of the geometry rank of the anomaly sources to start with the new imaging algorithm. The new EMT method is indeed related only to the pure physical aspects of the diffusion of EM waves underground and to the way the reflected waves are detected by the sensors located on the earth's surface. We deal with the EMT problem from a probabilistic point of view, as the search for a deterministic description of the buried structures is, in principle, an ill-posed problem and hence a rather limited approach.

Mailing address: Dr. Paolo Mauriello, Istituto per le Tecnologie Applicate ai Beni Culturali, CNR, Via Salaria km 29,300, 00016 Monterotondo St., Roma, Italy; e-mail: mauri@na.infn.it

In the development of the new EMT method, we follow the basic principles of the physical tomography recently proposed to analyse Self-Potential (SP) data (Patella, 1997).

2. The EM induction field

A Cartesian coordinate reference system x, y, z is taken with the x, y-plane representing the air-earth boundary and the z-axis positive downward into the earth. The rock parameters are assumed to be isotropic and the displacement currents are neglected. No impressed time-varying current sources are assumed to exist in the subsoil. Further, the magnetic permeability of rocks is assumed equal to that of free space, μ_0. Accordingly, Maxwell's equations are written as

$$\nabla \times \boldsymbol{h}(\boldsymbol{r},t) = \boldsymbol{j}(\boldsymbol{r},t), \tag{2.1}$$

$$\nabla \times \boldsymbol{e}(\boldsymbol{r},t) = -\mu_0 \frac{\partial \boldsymbol{h}(\boldsymbol{r},t)}{\partial t}, \tag{2.2}$$

$$\nabla \cdot \boldsymbol{j}(\boldsymbol{r},t) = 0, \tag{2.3}$$

$$\nabla \cdot \boldsymbol{h}(\boldsymbol{r},t) = 0, \tag{2.4}$$

where $\boldsymbol{j}(\boldsymbol{r}, t)$, $\boldsymbol{e}(\boldsymbol{r}, t)$ and $\boldsymbol{h}(\boldsymbol{r}, t)$ are the current density, the electric and the magnetic field vectors at point $\boldsymbol{r}$ and time t, respectively.

The null divergence condition for the current density in an inhomogenous medium, where $\boldsymbol{e}(\boldsymbol{r}, t)$ and $\boldsymbol{j}(\boldsymbol{r}, t)$ are linearly related through the resistivity parameter ρ by Ohm's law, leads to

$$\nabla \cdot \boldsymbol{e}(\boldsymbol{r},t) = \frac{\boldsymbol{e}(\boldsymbol{r},t) \cdot \nabla \rho}{\rho} \tag{2.5}$$

Due to the properties (2.2) and (2.4), a vector and scalar potential, $\boldsymbol{a}_0(\boldsymbol{r}, t)$ and $\phi_0(\boldsymbol{r}, t)$, respectively, can be introduced such that

$$\boldsymbol{h}(\boldsymbol{r},t) = \nabla \times \boldsymbol{a}_0(\boldsymbol{r},t). \tag{2.6}$$

$$\boldsymbol{e}(\boldsymbol{r},t) = -\nabla \phi_0(\boldsymbol{r},t) - \mu_0 \frac{\partial \boldsymbol{a}_0(\boldsymbol{r},t)}{\partial t}. \tag{2.7}$$

Since the EM field vectors must be invariant to any gauge transformation of the vector and scalar potential functions, any new pair $(\boldsymbol{a}, \phi)$ related to $(\boldsymbol{a}_0, \phi_0)$ by the gauge transformation

$$\boldsymbol{a}(\boldsymbol{r},t) = \boldsymbol{a}_0(\boldsymbol{r},t) - \frac{\nabla \lambda(\boldsymbol{r},t)}{\mu_0}, \tag{2.8}$$

$$\phi(\boldsymbol{r},t) = \phi_0(\boldsymbol{r},t) + \frac{\partial \lambda(\boldsymbol{r},t)}{\partial t}, \tag{2.9}$$

where $\lambda(\boldsymbol{r}, t)$ is an arbitrary scalar function, describes exactly the same EM field, *i.e.*

$$\boldsymbol{e}(\boldsymbol{r},t) = -\nabla \phi(\boldsymbol{r},t) - \mu_0 \frac{\partial \boldsymbol{a}(\boldsymbol{r},t)}{\partial t}, \tag{2.10}$$

$$\boldsymbol{h}(\boldsymbol{r}, t) = \nabla \times \boldsymbol{a}(\boldsymbol{r}, t). \tag{2.11}$$

Among all choices of $\boldsymbol{a}_0(\boldsymbol{r}, t)$ and $\lambda(\boldsymbol{r}, t)$, we assume that satisfying the condition

$$\nabla^2 \lambda(\boldsymbol{r},t) = \mu_0 \nabla \cdot \boldsymbol{a}_0(\boldsymbol{r},t), \tag{2.12}$$

which shifts the EM problem to the so-called *Coulomb gauge*, in which it is

$$\nabla \cdot \boldsymbol{a}(\boldsymbol{r},t) = 0. \tag{2.13}$$

It is easy to prove that $\boldsymbol{a}(\boldsymbol{r}, t)$ and $\phi(\boldsymbol{r}, t)$ satisfy Poisson's differential equation, *i.e.*

$$\nabla^2 \boldsymbol{a}(\boldsymbol{r},t) = -\boldsymbol{j}(\boldsymbol{r},t), \tag{2.14}$$

$$\nabla^2 \phi(\boldsymbol{r},t) = -\frac{\boldsymbol{e}(\boldsymbol{r},t) \cdot \nabla \rho}{\rho}, \tag{2.15}$$

which have solutions of the form

$$\boldsymbol{a}(\boldsymbol{r},t) = \frac{1}{4\pi} \int_V \frac{\boldsymbol{j}(\boldsymbol{r}',t)}{|\boldsymbol{r}-\boldsymbol{r}'|} dV, \tag{2.16}$$

$$\phi(\boldsymbol{r},t) = \frac{1}{4\pi} \int_V \frac{\boldsymbol{e}(\boldsymbol{r}',t) \cdot \nabla \rho}{|\boldsymbol{r}-\boldsymbol{r}'|\rho} dV. \tag{2.17}$$

In eqs. (2.16) and (2.17), V is the total volume where induced electric charges and currents generating the observed EM field exist, and $\boldsymbol{r}'$ gives the position of a generic point of V.

The sources of the vector potential are located in all regions where there is a non-vanishing current density, while those of the scalar potential are found in all places where there is a non-vanishing component of the resistivity gradient along the direction of the electric field. In the case of sharp resistivity contrasts, such places are the discontinuity surfaces.

Introducing the volume electrical dipole moment $\boldsymbol{p}(\boldsymbol{r}', t)$ and the surface electric charge intensity $\gamma(\boldsymbol{r}', t)$, the vector and scalar potentials at a generic observation point $\boldsymbol{r}$ can be approximated by a superposition of elementary contributions. In expanding the vector potential $\boldsymbol{a}(\boldsymbol{r}, t)$, the volume V is subdivided into M contiguous volume elements, covering the whole finite space of influence of the electrical dipole moment distribution over the observation point. In each mth volume element, we consider the average dipole moment, which is assigned to the point $\boldsymbol{r}_m$. Accordingly, the resistivity discontinuity total surface S is divided into N surface elements. In each nth surface element, we consider the average charge intensity, which is supposed to be located in the point $\boldsymbol{r}_n$. Hence, the vector and scalar potentials are approximated as

$$\boldsymbol{a}(\boldsymbol{r},t) \cong \sum_{m=1}^{M} \boldsymbol{a}_m(\boldsymbol{r},t) = \frac{1}{4\pi}\frac{\partial}{\partial t}\sum_{m=1}^{M}\frac{\boldsymbol{p}_m(t)}{|\boldsymbol{r}-\boldsymbol{r}_m|}, \tag{2.18}$$

$$\phi(\boldsymbol{r},t) \cong \sum_{n=1}^{N} \phi_n(\boldsymbol{r},t) = \frac{1}{4\pi\varepsilon_0}\sum_{n=1}^{N}\frac{\gamma_n(t)}{|\boldsymbol{r}-\boldsymbol{r}_n|}. \tag{2.19}$$

Using eqs. (2.10) and (2.11), we readily write the electric and magnetic field vectors as follows

$$\boldsymbol{e}(\boldsymbol{r},t) = \frac{1}{4\pi\varepsilon_0}\sum_{n=1}^{N}\frac{\gamma_n(t)}{|\boldsymbol{r}-\boldsymbol{r}_n|^3}(\boldsymbol{r}-\boldsymbol{r}_n) - \frac{\mu_0}{4\pi}\frac{\partial^2}{\partial t^2}\sum_{m=1}^{M}\frac{\boldsymbol{p}_m(t)}{|\boldsymbol{r}-\boldsymbol{r}_m|}, \tag{2.20}$$

$$\boldsymbol{h}(\boldsymbol{r},t) = \frac{1}{4\pi}\frac{\partial}{\partial t}\sum_{m=1}^{M}\nabla\times\frac{\boldsymbol{p}_m(t)}{|\boldsymbol{r}-\boldsymbol{r}_m|} \tag{2.21}$$

From now onward, we formulate the theory in the frequency-domain, assuming that the EM field has a $e^{i\omega t}$ time behaviour, with ω the angular frequency. Capital letters will be used to indicate the spectral amplitudes.

In the frequency-domain eqs. (2.20) and (2.21) become

$$\boldsymbol{E}(\boldsymbol{r}) = \frac{1}{4\pi\varepsilon_0}\sum_{n=1}^{N}\frac{\Gamma_n}{|\boldsymbol{r}-\boldsymbol{r}_n|^3}(\boldsymbol{r}-\boldsymbol{r}_n) + \frac{\mu_0\omega^2}{4\pi}\sum_{m=1}^{M}\frac{\boldsymbol{P}_m}{|\boldsymbol{r}-\boldsymbol{r}_m|}, \tag{2.22}$$

$$\boldsymbol{H}(\boldsymbol{r}) = \frac{i\omega}{4\pi}\sum_{m=1}^{M}\nabla\times\frac{\boldsymbol{P}_m}{|\boldsymbol{r}-\boldsymbol{r}_m|}, \tag{2.23}$$

from which we obtain the components of the EM field on the ground surface ($z = 0$) as

$$E_x(x,y) = \frac{1}{4\pi\varepsilon_0}\sum_{n=1}^{N}\frac{\Gamma_n(x-x_n)}{|\boldsymbol{r}-\boldsymbol{r}_n|^3}\Bigg|_{z=0} + \frac{\mu_0\omega^2}{4\pi}\sum_{m=1}^{M}\frac{P_{x,m}}{|\boldsymbol{r}-\boldsymbol{r}_m|}\Bigg|_{z=0}, \tag{2.24}$$

$$E_y(x,y) = \frac{1}{4\pi\varepsilon_0}\sum_{n=1}^{N}\frac{\Gamma_n(y-y_n)}{|\boldsymbol{r}-\boldsymbol{r}_n|^3}\Bigg|_{z=0} + \frac{\mu_0\omega^2}{4\pi}\sum_{m=1}^{M}\frac{P_{y,m}}{|\boldsymbol{r}-\boldsymbol{r}_m|}\Bigg|_{z=0}, \tag{2.25}$$

$$H_x(x,y) = \frac{i\omega}{4\pi}\sum_{m=1}^{M}\nabla\times\frac{\boldsymbol{P}_m}{|\boldsymbol{r}-\boldsymbol{r}_m|}\Bigg|_x\Bigg|_{z=0}, \tag{2.26}$$

$$H_y(x,y) = \frac{i\omega}{4\pi}\sum_{m=1}^{M}\nabla\times\frac{\boldsymbol{P}_m}{|\boldsymbol{r}-\boldsymbol{r}_m|}\bigg|_y\bigg|_{z=0}, \qquad (2.27)$$

$$H_z(x,y) = \frac{i\omega}{4\pi}\sum_{m=1}^{M}\nabla\times\frac{\boldsymbol{P}_m}{|\boldsymbol{r}-\boldsymbol{r}_m|}\bigg|_z\bigg|_{z=0}. \qquad (2.28)$$

From now onward, we will deliberately not consider the induction term in eq. (2.22). This neither means that we arbitrarily assume that this term is always negligible, which is of course not true, nor that we want to restrict the analysis within the low-frequency approximation. The rationale of the tomographic approach, already established by Patella (1997), permits us, in principle, to decide beforehand which contribution of a given field is to be scanned and thence to analyse only the response due to that contribution. In particular, for reasons that will be clarified later, in the study of each of the electric components given in eqs. (2.24) and (2.25), we shall be concerned only with the first contribution that relates to the charge distribution over the resistivity discontinuity surfaces. This restriction simply follows from the impossibility to deal with the induction term in the frame of the tomography imaging algorithm we are going to present. Nevertheless, this will be shown to be not a shortage of this new method, since the information that will be derived is coherent with the basic physics of the EM induction phenomenology.

3. The 2D analysis

We consider a generic 2D structure striking parallel to the y-axis and analyse the EM field along a profile perpendicular to the strike, *i.e.* parallel to the x-axis. For reasons that will clarified later, we deal only with the secondary EM field associated with the 2D structure. In practice, a secondary field can always be calculated by subtracting from the observed total field a primary field due to a background reference structure.

Assuming now that N and M represent a set of elementary strips and parallelepipeds both elongated in the y-direction, respectively, the first term in eqs. (2.24) and (2.25) of the electrical field components can be rewritten as

$$E_x(x) = \frac{1}{4\pi\varepsilon_0}\sum_{n=1}^{N}\int_{-\infty}^{+\infty}\Lambda_n\,\ell_x(x-x_n, y', z_n)\,dy' = \qquad (3.1)$$

$$= \frac{1}{2\pi\varepsilon_0}\sum_{n=1}^{N}\frac{\Lambda_n(x-x_n)}{(x-x_n)^2+z_n^2},$$

$$E_y(x) = \frac{1}{4\pi\varepsilon_0}\sum_{n=1}^{N}\int_{-\infty}^{+\infty}\Lambda_n\,\ell_y(x-x_n, y', z_n)\,dy' = 0, \qquad (3.2)$$

where

$$\ell_u(x-x_n, y-y_n, z_n) = \frac{(u-u_n)}{|\boldsymbol{r}-\boldsymbol{r}_n|^3} = \qquad (3.3)$$

$$= \frac{(u-u_n)}{[(x-x_n)^2+(y-y_n)^2+z_n^2]^{3/2}}, \quad u = x, y,$$

and Λ_n is the electric charge linear density.

As concerns the magnetic field, performing the integration of eqs. (2.26), (2.27) and (2.28) along the y-axis and introducing the dipole moments per unit length $\Theta_{v,m}(v = x, y, z)$, we obtain

$$H_y(x) = -\frac{i\omega}{2\pi}\sum_{m=1}^{M}\frac{\Theta_{y,m}z_m}{(x-x_m)^2+z_m^2}, \qquad (3.4)$$

$$H_x(x) = \frac{i\omega}{2\pi}\sum_{m=1}^{M}\frac{\Theta_{x,m}z_m+\Theta_{z,m}(x-x_m)}{(x-x_m)^2+z_m^2}, \qquad (3.5)$$

$$H_z(x) = -\frac{i\omega}{2\pi}\sum_{m=1}^{M}\frac{\Theta_{y,m}(x-x_m)}{(x-x_m)^2+z_m^2}. \qquad (3.6)$$

4. Probability tomography

4.1. *The source occurrence probability functions*

Eqs. (3.1) and (3.4) through (3.6) definitely allow us to realise the *EM tomography* similar to that proposed by Patella (1997) for the SP method. The goal is the evaluation of the distribution, along any x-z cross-section, of the occurrence probabilities of electric surface charges and current volume dipoles induced by the primary incident EM field, knowing their effects on the ground surface.

4.2. *Analysis of the electric field*

We first study the x-component of the electric field, which corresponds to the polarisation E-perpendicular to strike or TM mode. We introduce its spectral power density along any selected x-profile as

$$\int_{-\infty}^{+\infty} E_x^2(x)dx =$$

$$= \frac{1}{2\pi\varepsilon_0}\sum_{n=1}^{N}\Lambda_n\int_{-\infty}^{+\infty}E_x(x)\frac{(x-x_n)}{(x-x_n)^2+z_n^2}dx + \tag{4.1}$$

+ terms depending on dipole moments.

The nature of the secondary EM field, as previously outlined, always warrants convergence of the integral at the left-hand side of eq. (4.1).

To infer the electrical charge distribution directly from the measured electric field in the most objective way, we proceed as follows (Patella, 1997). We take any of the integrals of the sum at the right-hand side of eq. (4.1) and apply the cross-correlation bounding inequality (Bendat and Piersol, 1986)

$$\left[\int_{-\infty}^{+\infty}E_x(x)\Im_x(x-x_n,z_n)dx\right]^2 \le \tag{4.2}$$

$$\le \int_{-\infty}^{+\infty}E_x^2(x)dx\int_{-\infty}^{+\infty}\Im_x^2(x,z_n)dx.$$

We define as *space domain electric tomographic scanner* the function

$$\Im_x(x-x_n,z_n) = \frac{(x-x_n)}{(x-x_n)^2+z_n^2}. \tag{4.3}$$

It can be easily demonstrated that

$$\int_{-\infty}^{+\infty}E_x^2(x)dx\int_{-\infty}^{+\infty}\Im_x^2(x,z_n)dx = \frac{1}{C_x^2 z_n}, \quad z_n > 0, \tag{4.4}$$

where

$$C_x = \frac{\sqrt{2}}{\sqrt{\pi\int_{-\infty}^{+\infty}E_x^2(x)dx}}. \tag{4.5}$$

We now define the 2D Electric Charge Occurrence Probability (ECOP) function as

$$\eta_x^E(x_n,z_n) = C_x\sqrt{z_n}\int_{-\infty}^{+\infty}E_x(x)\Im_x(x-x_n,z_n)dx, \tag{4.6}$$

$$\text{for} \quad z_n > 0,$$

which obviously satisfies the condition

$$-1 \le \eta_x^E(x_n,z_n) \le 1. \tag{4.7}$$

The ECOP function allows us to have a detailed delineation of the charge dislocations underground. Positive values of $\eta_x^E(x_n, z_n)$ are the result of a major influence from positive charge accumulations, while negative values from negative charge clouds.

4.3. *Analysis of the magnetic field*

We study now the magnetic field and suppose again to work with the spectral amplitude evaluated along a profile on a flat ground surface at a fixed angular frequency ω.

The y-component of the magnetic field corresponds to the TM mode and is only due to the primary field. For this reason we consider only $H_x(x)$ and $H_z(x)$, *i.e.* the magnetic components in the polarisation H-perpendicular to strike or TE mode. Moreover, due to the polarisation of the electric field, the only non-vanishing dipole moment per unit length is $\Theta_{y,m}$. As for the electric field, we write the bounding inequality as

$$\left[\int_{-\infty}^{+\infty} H_v(x)\Re_v(x-x_m, z_m)dx\right]^2 \leq \tag{4.8}$$

$$\leq \int_{-\infty}^{+\infty} H_v^2(x)dx \cdot \int_{-\infty}^{+\infty} \Re_v^2(x, z_m)dx, \quad v = x, z,$$

where, according to eqs. (3.4) and (3.6), the space domain magnetic tomographic scanning function is given as

$$\Re_v(x-x_m, z_m) = \frac{-\delta_{v,x} z_m - \delta_{v,z}(x-x_m)}{(x-x_m)^2 + z_m^2}, \tag{4.9}$$

$$v = x, z,$$

where δ_{ij} is the Kronecker symbol which is equal to one if $i = j$ and zero elsewhere.

Similarly to the procedure used for the electric field, in this case we define an Electric Dipole Occurrence Probability (EDOP) function as

$$\eta_v^H(x_m, z_m) = \tag{4.10}$$

$$= C_v \sqrt{z_m} \int_{-\infty}^{+\infty} H_v(x)\Re_v(x-x_m, z_m)\,dx,$$

$$v = x, z, \quad z_m > 0,$$

where

$$C_v = \frac{\sqrt{2}}{\sqrt{\pi \int_{-\infty}^{+\infty} H_v^2(x)\,dx}}, \quad v = x, z.$$

4.4. *The tomographic procedure*

Following Patella (1997), the tomographic approach consists in a scanning procedure operated over the true field data functions by the space domain scanning functions, given in eq. (4.3) for the electric field and eq. (4.9) for the magnetic field.

We use an elementary positive source (electric charge or dipole) with unit strength to scan the whole subsoil to search where the induced sources are located. The result of the calculation of the cross-correlations 40 and 44 relative to a point P gives the probability that a positive (> 0) or negative (< 0) source (for the electric dipole the sign will identify the dipole direction) is located at P and is responsible for the observed EM field. We repeat the procedure for a set of grid points inside the investigated volume where the presence of induced EM sources is likely to exist.

Moreover, we realise a tomography for a set of values of ω for which the EM field components have non-vanishing amplitudes. These frequencies can be virtually selected in relation to the expected depths of the targets one wants to study, observing that for a fixed ω, the contribution coming from depths greater than the skin-depth is rapidly fading.

5. Synthetic examples

5.1. *First example*

The first 2D example regards an elongated prismatic body with rectangular cross-section of 7 km of width and 1.5 km of height, and with the top surface buried at 1.5 km of depth. The resistivity of the 2D body is 10 $\Omega \cdot$ m and that of the hosting half space is 100 $\Omega \cdot$ m.

Figure 1 shows the complete set of tomographies for the case of electric field perpendicular to strike (pictures e_1 through e_{14}), compared with the classical pseudosection (picture e_0). The positive direction of the electric fields is from left to right. For this as for all the other examples, the fourteen tomographies have been computed at the following frequencies in Hz: 160, 63, 25, 10, 4, 1.6, 0.63, 0.25, 0.1, 0.04, 0.016, 0.0063, 0.0023, 0.001.

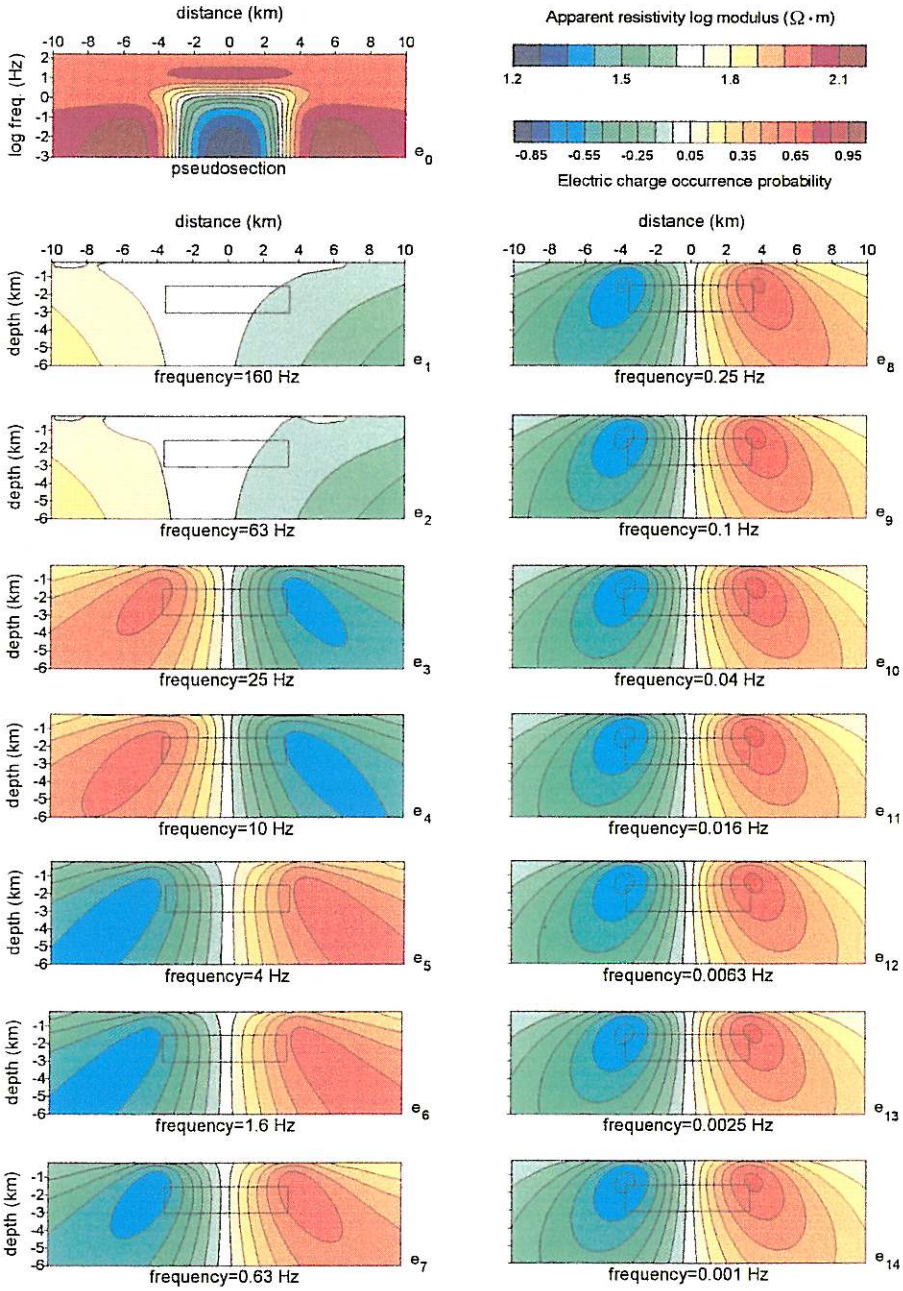

Fig. 1. Electromagnetic physical tomographies (pictures e_1 through e_{14}) compared with the classical pseudosection (picture e_0) for the synthetic case of an elongated prismatic body with rectangular cross-section of 7 km of width and 1.5 km of height, and with the top surface buried at 1.5 km of depth. The resistivity of the 2D body is 10 $\Omega \cdot$ m and that of the hosting half-space is 100 $\Omega \cdot$ m. The figure refers to the case of electric field perpendicular to strike.

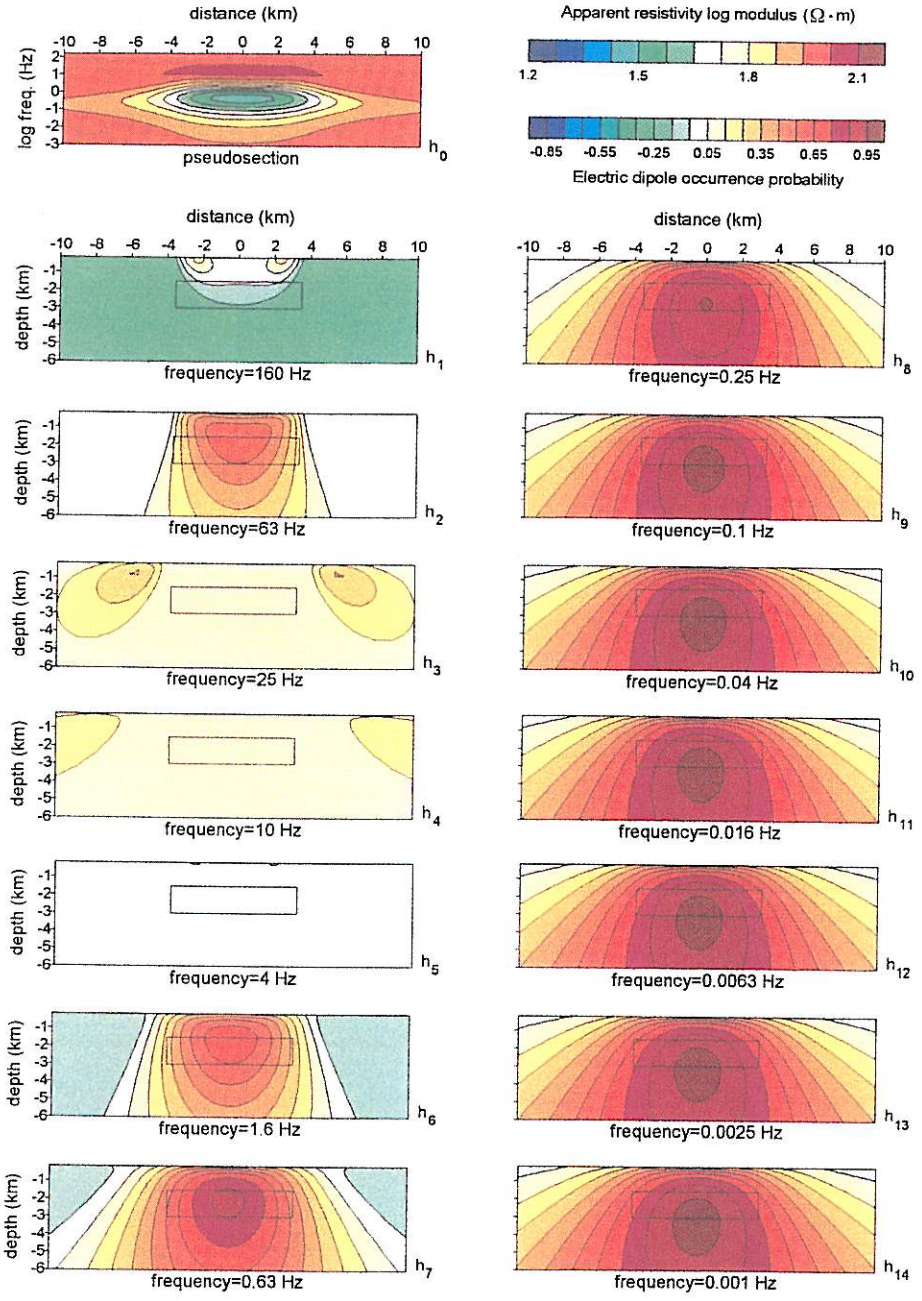

Fig. 2. Electromagnetic physical tomographies (pictures h_1 through h_{14}) compared with the classical pseudosection (picture h_0) for the synthetic case of an elongated prismatic body with rectangular cross-section of 7 km of width and 1.5 km of height, and with the top surface buried at 1.5 km of depth. The resistivity of the 2D body is 10 Ω · m and that of the hosting half-space is 100 Ω · m. The figure refers to the case of magnetic field perpendicular to strike.

We do not observe any significant anomaly in the pseudosection starting from the top frequency of 160 Hz down to a frequency of about 30 Hz. For this reason, pictures e_1 and e_2, which represent the ECOP tomographies for frequency values of 160 Hz and 63 Hz, respectively, do not show any neat source configuration.

In the frequency range 30-10 Hz a maximum of apparent resistivity is evident in the pseudosection. Physically speaking, this effect is due to charge accumulation on the resistivity discontinuities, mainly the vertical ones because of the polarisation direction, which determines an increase of the secondary electric field above the conductive prism. Pictures e_3 and e_4, relative to the frequency values of 25 Hz and 10 Hz, respectively, show an ECOP distribution with maximum values in correspondence of the vertical boundaries of the prism.

As frequency decreases, the EM wave penetrates the conductor and a new charge distribution develops on the lateral boundaries. This leads to a distortion of the electric field behaviour with a consequent apparent resistivity minimum in correspondence of the prism, which persists down to an arbitrary low frequency (Wannamaker *et al.*, 1984). Pictures e_5, e_6 and e_7 show a transient situation in which a new bipolar ECOP distribution is establishing. The sign reversal with respect to the two previous tomographic pictures is due to the birth of a new reversed charge accumulation, which generates the low electric field within the prism. As soon as the EM wave fully penetrates the prism, the electric charge set-up becomes asymptotically stable down to any low frequency limit, as pictures e_8 through e_{14} clearly show.

Accordingly, fig. 2 shows the complete set of tomographies for the case of magnetic field perpendicular to strike (pictures h_1 through h_{14}), compared again with the classical pseudosection (picture h_0).

As in the previous polarisation, we again observe in the pseudosection an apparent resistivity maximum above the frequency range in which the effect of the conductive prism becomes well evident. This effect is due to the crowding of current lines from regions overlying the prism as far as the frequency of the EM wave is not sufficiently low to fully penetrate the conductive body. This is represented in the tomographic pictures h_1 through h_4, where maxima of the EDOP distribution are well evident in the neighbourhood of the body and interest a wider and wider region as frequency decreases.

A narrow transition frequency band exists in which the magnetic effect due to the prism completely vanishes. This situation of complete transparency is well evident in the tomography of picture h_5 corresponding to the frequency of about 4 Hz.

Then, the EM wave begins to penetrate the prism. In particular, pictures h_7 and h_8, which refer to the frequencies of 0.63 Hz and 0.25 Hz, respectively, both related to the apparent resistivity minimum of picture h_0, show a maximum of the EDOP parameter exactly in correspondence with the body axis. A slight, nearly stable deepening of this maximum appears in all subsequent tomographic pictures. This can be explained as due to a combined effect of the current density inside and closely underlying the prism, since the frequency is now low enough to get the EM wave down, well beyond the body.

Figures 3 and 4 refer to the same prismatic model, but with reversed resistivity contrast, *i.e.* the 2D body is given a resistivity of 100 $\Omega \cdot$ m and the hosting half-space 10 $\Omega \cdot$ m. Essentially the same considerations as above can be still drawn about the significance of the most relevant probability contours, apart from an obvious sign reversal of the geometry tracing charge and dipole occurrence probability nuclei.

5.2. *Second example*

The second example regards a horst-like structure. It is an extension of the first example to the case in which the bottom level of the 2D prismatic body extends infinitely down. Again it is of 7 km of width and the top level stands at 1.5 km of depth. The resistivity of the 2D body is 10 $\Omega \cdot$ m and that of the hosting half space is 100 $\Omega \cdot$ m.

Figure 5 shows the complete set of tomographies (pictures e_1 through e_{14}) for the TM mode (electric field perpendicular to strike), compared as before with the standard pseudosection (picture e_0). The positive direction of the electric field is again from left to right. The frequencies

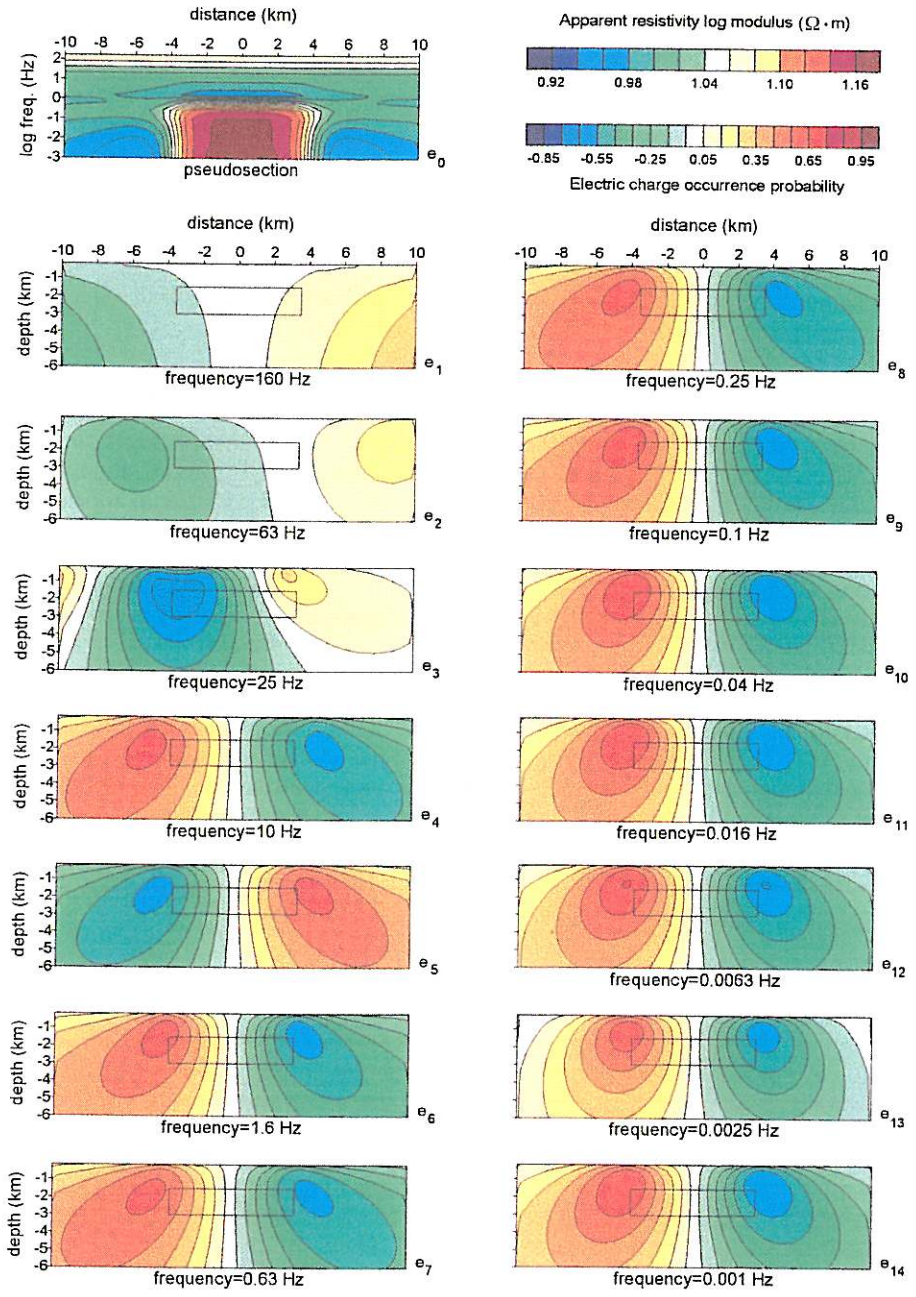

Fig. 3. Electromagnetic physical tomographies (pictures e_1 through e_{14}) compared with the classical pseudosection (picture e_0) for the synthetic case of an elongated prismatic body with rectangular cross-section of 7 km of width and 1.5 km of height, and with the top surface buried at 1.5 km of depth. The resistivity of the 2D body is 100 $\Omega \cdot$ m and that of the hosting half-space is 10 $\Omega \cdot$ m. The figure refers to the case of electric field perpendicular to strike.

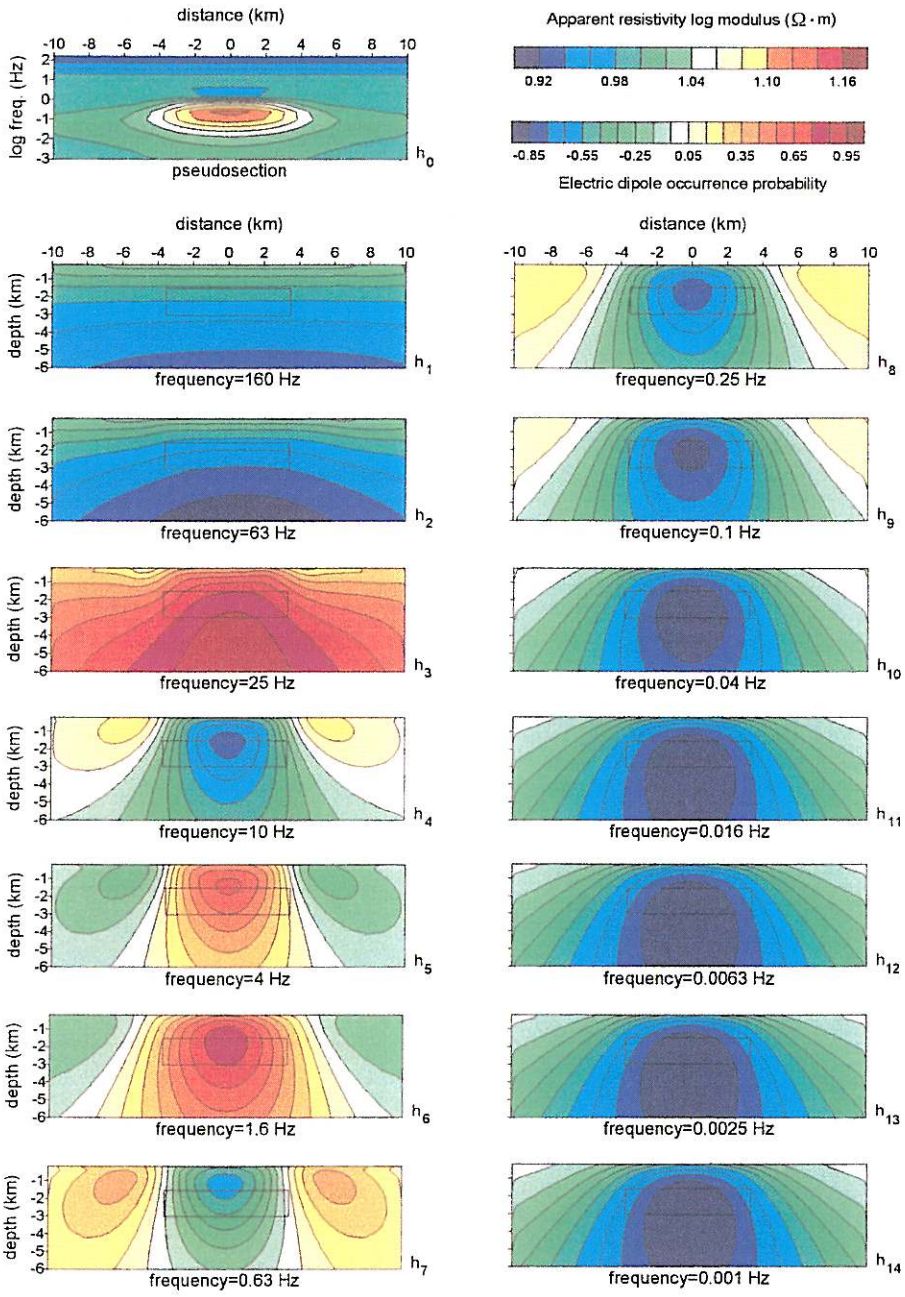

Fig. 4. Electromagnetic physical tomographies (pictures h_1 through h_{14}) compared with the classical pseudosection (picture h_0) for the synthetic case of an elongated prismatic body with rectangular cross-section of 7 km of width and 1.5 km of height, and with the top surface buried at 1.5 km of depth. The resistivity of the 2D body is 100 Ω · m and that of the hosting half-space is 10 Ω · m. The figure refers to the case of magnetic field perpendicular to strike.

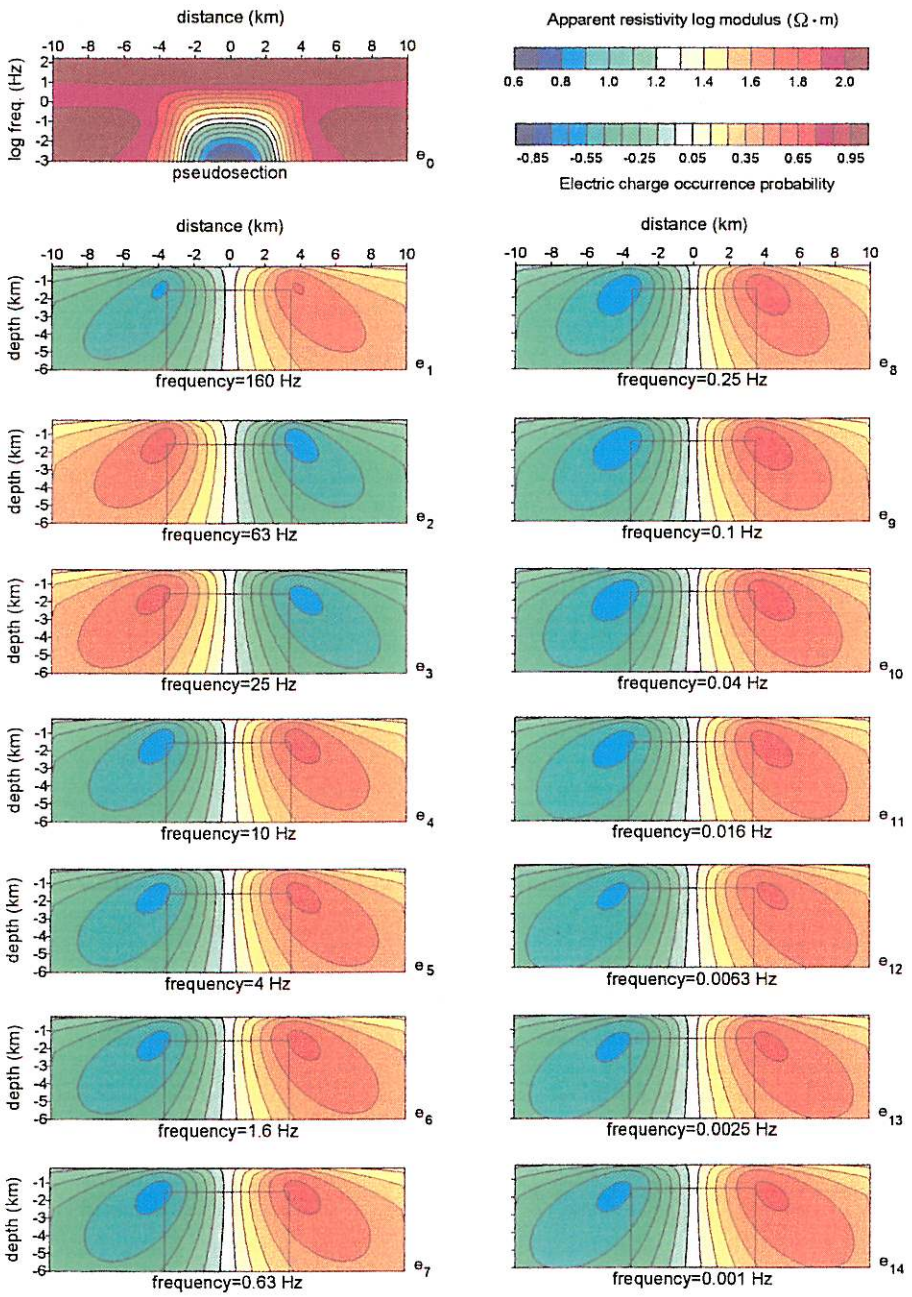

Fig. 5. Electromagnetic physical tomographies (pictures e_1 through e_{14}) compared with the classical pseudosection (picture e_0) for the synthetic case of an elongated horst-like prismatic body with 7 km of width and with the top surface buried at 1.5 km of depth. The resistivity of the 2D body is 10 Ω·m and that of the hosting half-space is 100 Ω·m. The figure refers to the case of electric field perpendicular to strike.

at which the tomographies have been computed are the same as before.

Significant ECOP tomographies are this time seen even starting from the top frequency of 160 Hz until the lowest frequency. Again, sign reversals of the ECOP function are observed in the high frequency transition band, passing from picture e_1 to e_2 the first time and from picture e_3 to e_4 the second time, indicating as before reversed sign charge accumulations. In any case, in each picture the highest absolute values of the ECOP function are observed around the top lateral edges of the prismatic horst-like body, exactly at the depth of the top surface of the prism. The lateral spacing between the two reversed sign nucleuses always closely corresponds to the width of the body. The asymptotic stability is now reached very soon, practically from picture e_4 down to any low frequency limit, because this time there is not the influence of the bottom surface in modifying the tomographies.

Accordingly, fig. 6 shows the complete set of tomographies (pictures h_1 through h_{14}) for the TE mode (magnetic field perpendicular to strike) compared as usual with the standard pseudosection (picture h_0).

A transition frequency band again exists in which the EDOP imaging is far from having reached stability (see pictures h_1 through h_7), although clear signs of the presence of the prismatic body are this time well evident even in pictures h_3 and h_4. Once the EM waves begin to fully penetrate the prism, a maximum of the EDOP parameter appears exactly in correspondence with the body axis. Moreover, the EDOP maximum migrates downwards as frequency lowers, starting from picture h_8 until the last one, and the size of the EDOP nucleus also regularly spreads over a larger and larger parabolic surface. Both aspects can be explained as due to the infinite extension of the prism in depth.

5.3. *Third example*

The third example regards a fault model. The overlying resistivity is 100 $\Omega \cdot$ m and the underlying 10 $\Omega \cdot$ m. The depths of the two plateaux are 1 km and 2.5 km, respectively. Similar considerations as in the previous example can be again made.

Figure 7 refers to the case of electric field perpendicular to strike. In particular, picture e_0 shows the standard pseudosection and pictures e_1 through e_{14} the corresponding tomographies. Omitting the details concerning the first seven tomographies, which correspond to a transition frequency band from 160 Hz down to 0.63 Hz, we then observe a neat ECOP maximum appearing in pictures e_8 through e_{14} in close correspondence with the fault throw.

Very interesting features appear in the tomographies corresponding to the case of magnetic field perpendicular to strike, drawn in pictures h_1 through h_{14}, following the classical pseudosection of picture h_0 (fig. 8). The strongest anomalies in the pseudosection are evident in the frequency range from 4 Hz down to 0.63 Hz. The tomographies related to these frequencies are shown in pictures h_5, h_6 and h_7, respectively at 4, 1.6 and 0.63 Hz. A maximum EDOP value appears in the conductive side of the fault, close to the confining resistive side, which demonstrates a dense secondary current circulation. *Vice versa*, in the resistive side, the decrease of total current circulation is seen as a negative EDOP nucleus, which corresponds to an equally dense secondary current circulation in the opposite direction.

As frequency lowers, the EDOP maximum at the right-hand side of the sections tends to stabilise at a much greater depth with a much larger extension.

6. Conclusions

We have described a new tomographic approach for physical pattern recognition of 2D anomaly sources in the study of EM induction fields underground. The proposed method has the advantage that in principle no strict reference to the geometry of the anomaly sources is necessary as an *a priori* constraint to start with the imaging algorithm. It only relates to the true physical aspects of the EM wavefield diffusion process that emerge from the data collected above the air-earth interface.

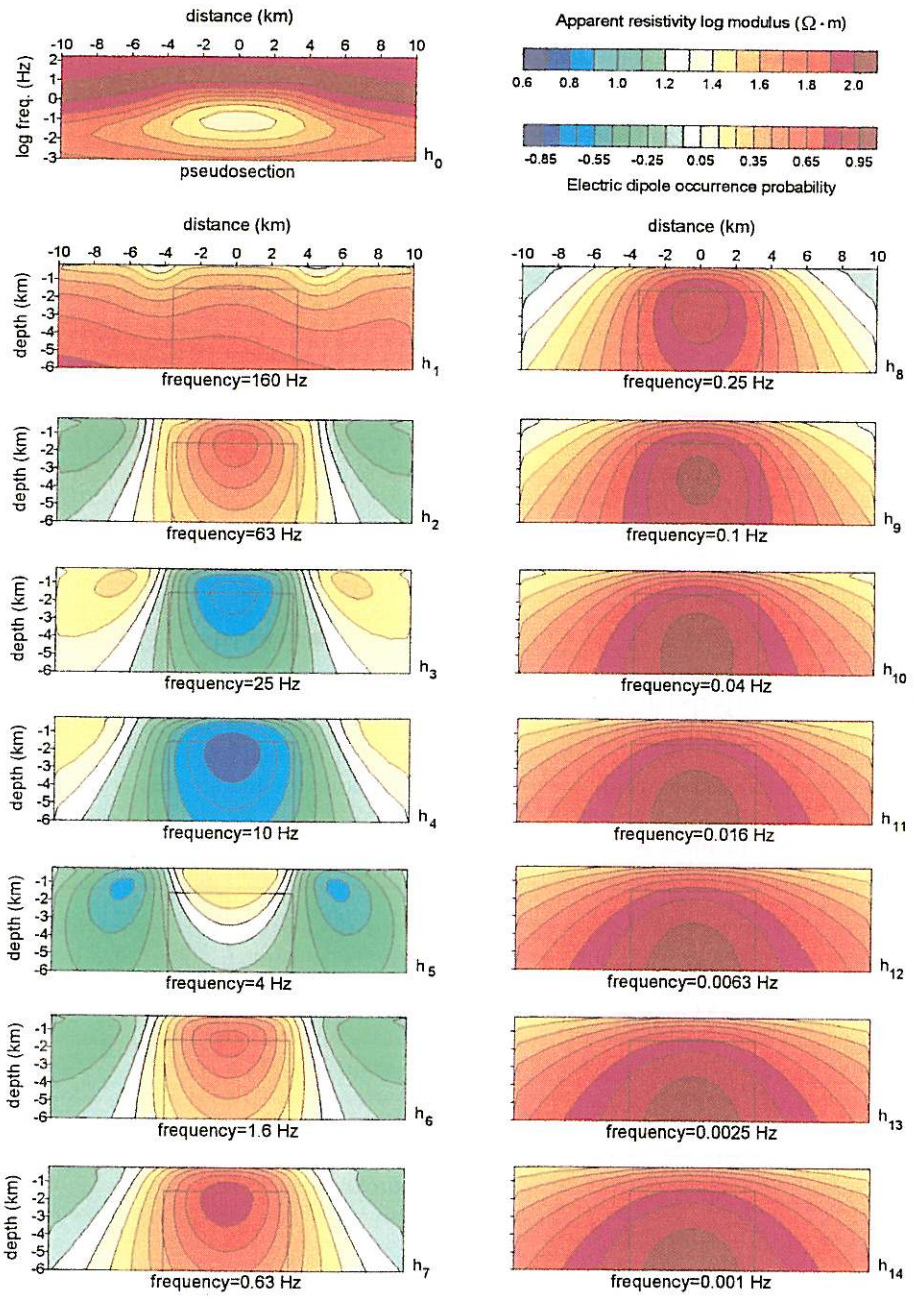

Fig. 6. Electromagnetic physical tomographies (pictures h_1 through h_{14}) compared with the classical pseudosection (picture h_0) for the synthetic case of an elongated horst-like prismatic body with 7 km of width and with the top surface buried at 1.5 km of depth. The resistivity of the 2D body is 10 Ω · m and that of the hosting half-space is 100 Ω · m. The figure refers to the case of magnetic field perpendicular to strike.

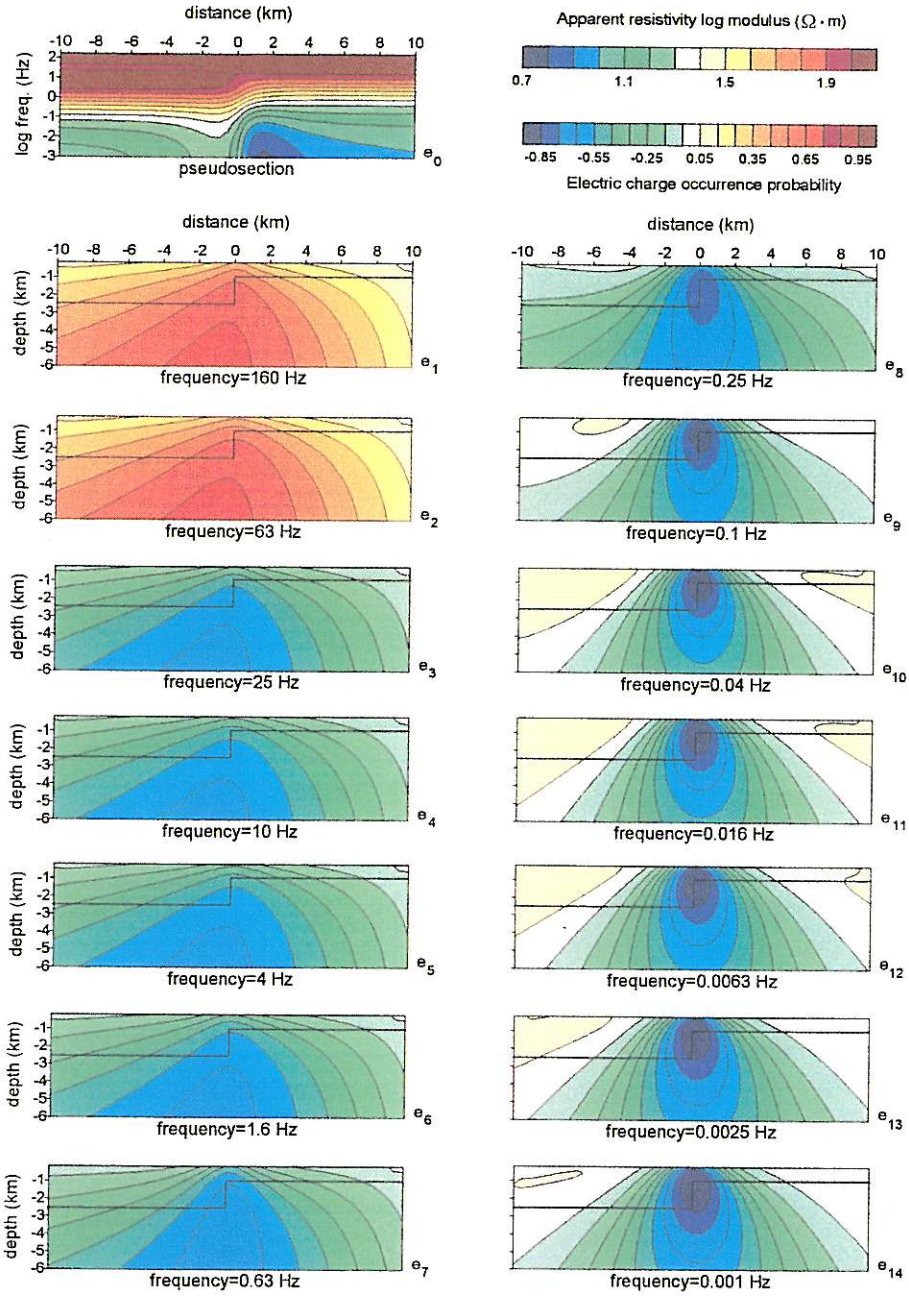

Fig. 7. Electromagnetic physical tomographies (pictures e_1 through e_{14}) compared with the classical pseudosection (picture e_0) for the synthetic case of a faulted geometry. The overlying resistivity is 100 Ω · m and the underlying 10 Ω · m. The depths of the two plateaux are 1 km and 2.5 km, respectively. The figure refers to the case of electric field perpendicular to strike.

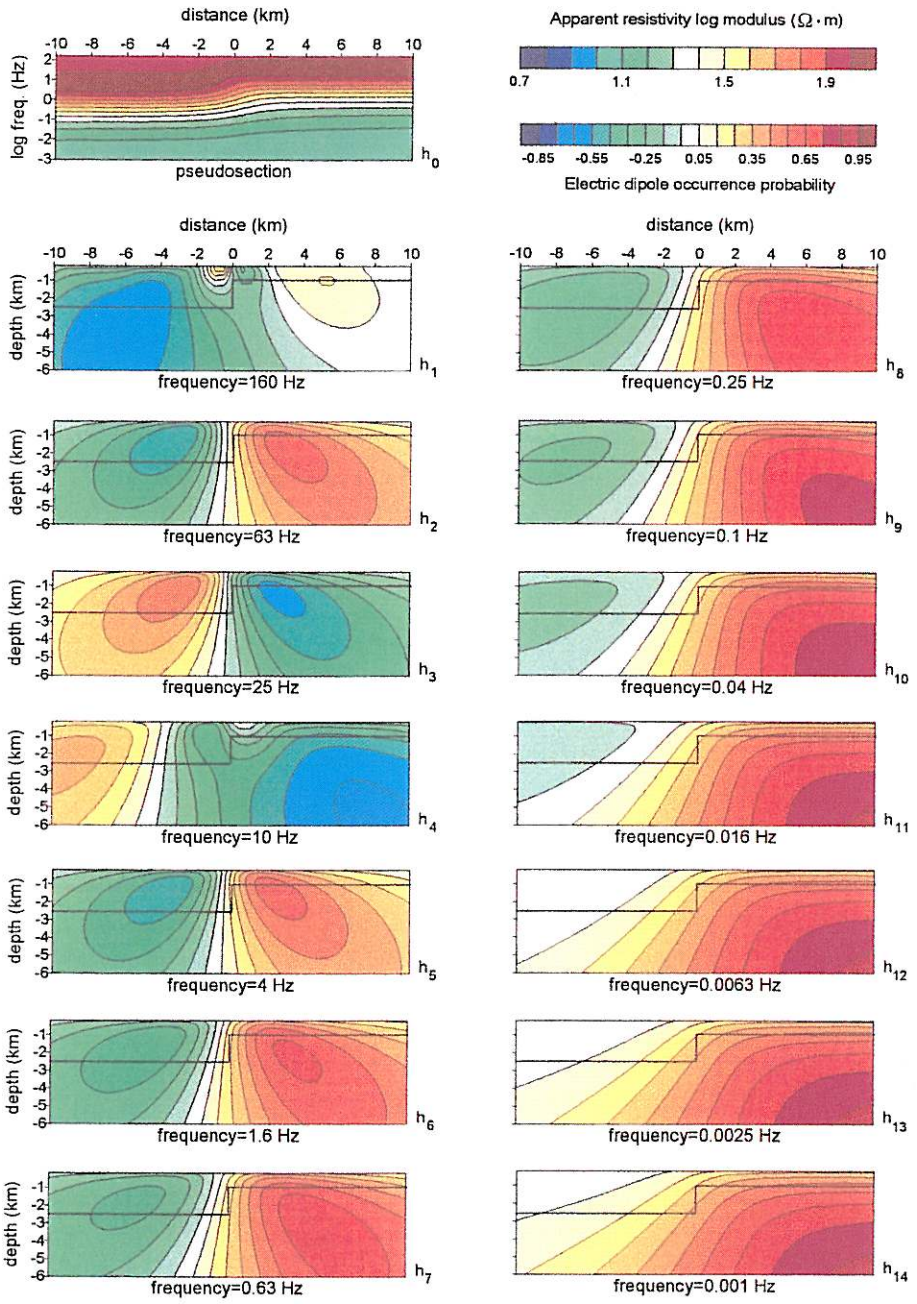

Fig. 8. Electromagnetic physical tomographies (pictures h_1 through h_{14}) compared with the classical pseudosection (picture h_0) for the synthetic case of a faulted geometry. The overlying resistivity is 100 Ω · m and the underlying 10 Ω · m. The depths of the two plateaux are 1 km and 2.5 km, respectively. The figure refers to the case of magnetic field perpendicular to strike.

The rationale underlying the new EMT method is the simultaneous computation of the occurrence probabilities of both electric charges and current dipoles underground. The ECOP and EDOP tomographies together constitute a complete physical and geometrical pattern recognition approach across vertical sections. Physically speaking, polarised electric charges are surface effects, that for down travelling waves are essentially distributed around the uppermost edges of any 2D anomalous body, while polarised current dipoles are volume effects concentrated inside conductive structures. Among these structures we must of course include also those disturbing bodies that generate unwanted static shift effects. Polarized electric charge and current dipoles associated with these bodies cannot in principle be distinguished, unless the static shift effects are eliminated beforehand using any standard correction method.

The use of probability parameters for EM pattern recognition is thought to be unavoidable. Indeed, due to intrinsic equivalence and noise contamination from cultural and/or natural external sources, the search for a deterministic solution of the true physical and geometrical configuration of the buried perturbative structures has basically much less common-sense than is believed.

REFERENCES

BENDAT, J.A.S. and A.G. PIERSOL (1986): *Random Data: Analysis and Measurement Procedures* (John Wiley & Sons), pp. 566.

EATON, P.A. (1989): 3D electromagnetic inversion using integral equations, *Geophys. Prospect.*, **37**, 407-426.

LEE, S., G.A. MCMECHAN and C.L.V. AIKEN (1987): Phase-field imaging: The electromagnetic equivalent of seismic migration, *Geophysics*, **52**, 678-693.

LEE, K.H., G. LIU and H.F. MORRISON (1989): A new approach to modeling the electromagnetic response of conductive media, *Geophysics*, **54**, 1180-1192.

PATELLA, D. (1997): Introduction to ground surface self-potential tomography, *Geophys. Prospect.*, **45**, 653-681.

POULTON, M.M., B.K. STERNBERG and C.E. GLASS (1992): Location of subsurface targets in geophysical data using neural networks, *Geophysics*, **57**, 1534-1544.

SASAKI, Y. (1989): Two-dimensional joint inversion of magnetotelluric and dipole-dipole resistivity data, *Geophysics*, **54**, 254-262.

SASAKI, Y., K. MATSUO and K. YOKOI (1994): Resistivity inversion of cross-hole and borehole-to-surface EM data using axially symmetric models, *Geophys. Prospect.*, **42**, 745-754.

WANNAMAKER, P.E., G.W. HOHMANN and S.H. WARD (1984): Magnetotelluric responses of three-dimensional bodies in layered earth, *Geophysics*, **49**, 1517-1533.

ZHDANOV, M.S., P. TRAYNIN and J.R. BOOKER (1996): Underground imaging by frequency-domain electromagnetic migration, *Geophysics*, **61**, 666-682.

ZHOU, Q., A. BECKER and H.F. MORRISON (1993): Audio-frequency electromagnetic tomography in 2D, *Geophysics*, **58**, 482-495.